Journal of Materials Research and Technology 41 (2026) 1974–1985

Contents lists available at ScienceDirect

Journal of Materials Research and Technology

journal homepage: www.elsevier.com/locate/jmrt

Effects of substrate preheating and processing parameters on the crystallographic texture of Hastelloy X on SX-like Ni fabricated by L-PBF process with flat-top laser beam

Phuangphaga Daram *, Fabien Briffod, Tomonori Kitashima, Masahiro Kusano, Makoto Watanabe

Research Center for Structural Materials, National Institute for Materials Science, 1-2-1 Sengen, Tsukuba, Ibaraki, 305-0047, Japan

ARTICLE INFO

Keywords:
Hastelloy X
Laser powder bed fusion process
Substrate preheating
Microstructure
Texture
Stray grains

ABSTRACT

This work investigates the effects of substrate preheating and processing parameters on the crystallographic texture of Hastelloy X (HX) deposited on a single crystal (SX)-like Ni substrate using laser powder bed fusion (L-PBF) process. Single- and multi-track experiments together with HX deposited on SX-like Ni substrate, were examined under varying laser powers and scanning speeds, with substrate preheating applied using a flat-top beam. A heat transfer model was employed to simulate the thermal history of melt pool. The results showed that higher laser power and lower scanning speed, combined with substrate preheating, produced larger melt pools and promoted elongated columnar grains formation throughout the Z-direction. Increasing the linear energy density (LED) from 1.5 J/mm to 5 J/mm at substrate preheating of 200 °C reduced the temperature gradient (G) by approximately −16 %, as well as the solidification rate (R) and cooling rate (G × R) by −87 % and −89 %, respectively. These reductions in solidification kinetics promoted coarser primary dendrite arm spacing (PDAS), increasing from ~1.2 μm to ~2 μm. Moreover, substrate preheating improved metallurgical bonding and promoted epitaxial columnar growth, resulting in a strong <001> texture extending from the SX-like Ni into the HX layers. Consequently, the multiple of uniform distribution (MUD) increased from 2.5 to 4 under higher energy density (E) with substrate preheating. The findings demonstrate that high E and substrate preheating effectively reduces G, R, and G × R, thereby enhancing texture control and improving process optimization for fabricating SX-like HX structures via the L-PBF process.

1. Introduction

Hastelloy X (HX) is well-known for its excellent high-temperature strength and oxidation resistance. These properties make it ideal for demanding applications, such as gas turbine parts and aerospace components [1,2]. Laser powder bed fusion (L-PBF) is an additive manufacturing (AM) technique that has emerged as a powerful method for producing complex three-dimensional (3D) structures. It offers exceptional design freedom, high resolution, and material efficiency, resulting in highly dense components [1]. Specifically, the rapid solidification and inherently non-equilibrium conditions of the L-PBF process promote the formation of a fine microstructure, thereby enhancing the mechanical and corrosion properties of the material [3]. In recent years, controlling the crystallographic texture in AM has become crucial for optimizing the mechanical and functional properties of 3D-printed metallic components [4]. Unlike conventional manufacturing methods, AM processes such as L-PBF, electron beam melting (EBM), and directed energy deposition (DED) provide unique opportunities to tailor grain morphology and orientation via layer-by-layer deposition and localized melting and solidification dynamics [5]. Nevertheless, achieving reliable and reproducible control over crystallographic texture remains a significant challenge in the additive manufacturing of metallic systems.

Texture formation in AM process is primarily governed by the epitaxial growth of grains from previously solidified layers into the melt pool. This process is strongly influenced by the local thermal history, particularly the temperature gradient (G) and the solidification growth rate (R). Both the ratio undercooling (G/R) and the product cooling rate (G × R) determine the solidification kinetics, grain size, and morphology [6–8]. During solidification, the preferential growth direction of

* Corresponding author.
E-mail address: daram.phuangphaga@nims.go.jp (P. Daram).

https://doi.org/10.1016/j.jmrt.2026.01.142
Received 12 November 2025; Received in revised form 4 January 2026; Accepted 19 January 2026
Available online 20 January 2026

columnar cells in face-centered cubic (fcc) and body-centered cubic (bcc) metals typically aligns with the <100> crystallographic orientation. Consequently, columnar grains tend to grow parallel to the heat-flow direction, which is nearly perpendicular to the tangential boundary of the melt pool [7,9].

Many studies have demonstrated strategies to control microstructural evolution during AM processes to achieve desirable mechanical performance [7–11]. Processing parameters such as laser power, scanning speed, scanning strategy and substrate preheating significantly affect grain evolution. These factors collectively promote continuous epitaxial growth from pre-existing grains while suppressing heterogeneous nucleation of new grains. Daram et al. reported that applying a higher energy input in L-PBF reduces the G × R, which increase cell and grain size in HX deposited alloy. This microstructural coarsening results in reduced microhardness and yield strength, but improves elongation in the L-PBF-processed HX alloy. Moreover, a lower temperature gradient favors epitaxial growth and columnar grain development, giving rise to both morphological and crystallographic textures along the build direction [12]. The Young's modulus of the L-PBF HX samples depends on the degree of crystallographic orientation, indicating that desired mechanical properties can be achieved by controlling processing parameters [4]. Montero-Sistiaga et al. presented that a flat-top power distribution from a high power laser during L-PBF of HX produced wide and shallow melt pools, which promoted the formation of morphological and crystallographic texture oriented along the build direction. Conversely, a low power laser with a Gaussian power profile generated narrow and deep melt pools, resulting in weaker texture intensity and grains orientations distributed not only along the build direction but also inclined at angles of 30–50° with respect to it [13]. Similarly, Jodi et al. observed that specimens produced using a Gaussian laser profile exhibited a higher density of geometrically necessary dislocations (GNDs) compared to those fabricated using a flat-top profile. The increased GND content led to greater cell-wall misorientation, which promoted stray grains formation and prevented continuous epitaxial <001> fcc growth along the build direction [14–16].

In some case, crystallographic texture control has been demonstrated by transitioning from columnar to single crystalline microstructure through the use of single crystal (SX) substrate [8,17,18]. SX substrate can promote epitaxial growth and eliminate the competitive growth region typically found at the bottom of the specimen, thereby saving both time and material. When SX substrate is used, the deposited material inherits the orientation of the seed crystal, stabilizing the crystallographic texture and minimizing stray grain formation. A synchrotron-based study by Xue et al. [17] revealed that depositing a Ni-based superalloy onto a directionally solidified substrate allowed epitaxial growth of columnar grains, while maintaining seamless crystalline orientation continuity across the interface. Likewise, Ishimoto et al. investigated that using a SX seed with controlled in-plane orientation enables stable epitaxial growth across subsequent layers; notably, aligning the <100> direction with the laser scanning direction strongly preserved texture continuity, even when the seed's orientation along the build direction varied [18]. Similarly, the SX CMSX-4 substrates used in L-PBF produced epitaxial SX deposits up to 500 μm in height, with potential to reach 1000 μm through fine-tuning of processing parameters [19]. Thin-wall structures fabricated by L-PBF from SX substrates exhibited exceptionally low misorientation (<3°), indicating near-perfect inheritance of the substrate's orientation along the build direction-affirming excellent epitaxial accuracy, as reported by Liu and Shu [20].

In addition, the substrate preheating is a critical parameter in AM process, as it directly influences residual stress mitigation, microstructural evolution, defect suppression, and the overall performance of the fabricated component [21–24]. From a microstructural perspective, substrate preheating promotes the coarsening of cellular substructure, reduce dislocation density, and enhances epitaxial grain growth by stabilizing favorable temperature gradients. Elevated preheating temperatures also accelerate atomic diffusion, thereby facilitating solute homogenization and reducing the tendency for porosity formation. For example, Chen et al. demonstrated that substrate preheating at 700 °C produced wider and deeper melt pools, which lowered G × R and reduced liquation cracking susceptibility. This condition also encouraged a more uniform temperature gradient, supporting the directional growth of columnar dendrites through the XZ plane [22]. Similarly, substrate preheating at 350 °C under identical laser parameters has been shown to increase melt pool width and depth, giving rise to a unique crystallographic lamellar microstructure (CLM) in LPBF-processed IN738LC superalloy. This CLM consisted of a <110> oriented major layer with <100>-oriented sublayer, both aligned the build direction [23]. Although the effects of preheating temperature have been investigated in previous studies, detailed insights into its influence on crystallographic texture remain limited. Therefore, careful selection of preheating temperature is particularly important for achieving controlled microstructural features and ensuring high-quality fabrication in additive manufacturing.

The primary objective of this study is to elucidate the effect of substrate preheating and SX substrates on the microstructural evolution and crystallographic texture of HX alloys fabricated by L-PBF process. The influence of processing parameters and substrate preheating on texture development is systematically investigated using a flat-top laser beam. To promote epitaxial growth and enable effective transfer of crystallographic orientation, single-crystal like Ni deposited seeds are employed as substrates. Furthermore, thermal history simulations are compared with experimental observations to provide a comprehensive understanding of the underlying mechanisms.

2. Experimental procedure

2.1. Single- and multi-tracks experiments

Fig. 1 illustrates a schematic of the experimental set-up for single- and multi-tracks fabrication without powder, as well as the deposit samples. The L-PBF experiments were conducted using an SLM Solution 280 L system, operated under an argon atmosphere with a purity exceeding 99.99 %. A 1000 W flat-top laser beam with a diameter of 700 μm was employed in conjunction with high temperature preheating platform.

In single- and multi-track experiments, laser scans were performed on polycrystalline HX substrate plate with dimensions of 50 mm × 50 mm and a thickness of approximately 2 mm. Prior to processing, the plates were polished to achieve a uniform surface finish. During the experiments, the powder was not spread, and thermocouple were attached to monitor the substrate temperature, which was maintained at a constant target value prior to single- and multi track scanning. Various combinations of laser power (P) and scanning speed (V) were applied for each track, as listed in Table 1. A total of 33 parameter conditions were investigated for the single-track experiments. Two single track experiment were tested for each condition to calculate the average. From these, two representative conditions-low energy density (P = 300 W, V = 200 mm/s) and high energy density (P = 1000 W, V = 250 mm/s)-each with varrying hatch spacing (h), were selected to fabricate multi-tracks. Thirty-three laser-remelted single tracks, each measuring 10 mm × 10 mm with 2 mm spacing, were produced as schematically illustrated in Fig. 1a. All experiments were conducted at different substrate preheating temperatures: room temperature (30 °C), 100 °C, 200 °C, 300 °C, and 400 °C.

The single- and multi-track specimens were sectioned perpendicular to the laser scanning direction followed by mounting, grinding and polishing. The polished cross-sections were then electrochemically etched using a 10 %oxalic acid solution for subsequent microstructural characterization. Optical microscope (OM; VHX series, Keyence) and scanning electron microscope (SEM; JSM-6010 LA, JEOL) analyzes were performed, along with electron backscatter diffraction (EBSD; JSM-

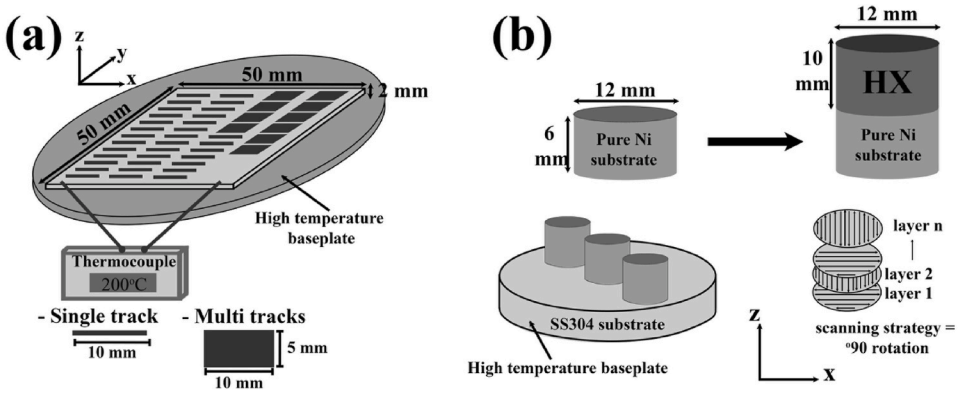

Fig. 1. Schematic diagram of (a) single- and multi-track experiments on a polycrystalline HX substrate equipped with a thermocouple and (b) the specimen design and experimental setup for HX deposition on Ni substrates.

Table 1
Process parameters used in the single-track experiment (LED; J/mm).

Scanning speed (mm/s)	Laser power (W)						
	200	300	400	500	600	700	1000
200	1	**1.5**	2	2.5	**3**	3.5	**5**
250		1.2	1.6	2	2.4	2.8	4
300		1	1.3	1.6	2	2.3	3.3
350			1.14	1.4	1.7	2	2.8
400			1	1.25	1.5	1.75	2.5
500				1	1.2	1.4	2

*Low LED => P = 300 W, V = 200 mm/s.
Medium LED => P = 600 W, V = 200 mm/s.
High LED => P = 1000 W, V = 200 mm/s.

Table 2
Process parameters use for HX deposition on SX-like Ni substrate (VED; J/mm^3).

Scanning speed (mm/s)	Laser power (W)					
	300	400	500	600	700	1000
200	**500**	666.7	833.3	**1000**	1166.7	**1666.7**
250		533.3	666.7	800	933.3	1333.3
300		444.4	555.6	666.7	777.8	1111
350			476.2	571.4	666.7	952.4
400			416.7	500	583.3	833.3
500				400	466.7	666.7

7200F, JEOL) operated at an accelerating voltage of 15 kV and a step size of 1 μm. Post-processing of EBSD data was carried out using the OIM Analysis™ (EDAX) software package to evaluate grain orientation, misorientation, and texture. Melt pool dimension, grain dimension, and primary dendrite spacing (PDAS) were measured using the *Image J* program (Fiji software).

2.2. HX deposited on Ni samples experiments

In deposited sample study, HX deposited on single crystal (SX)-like Ni substrate was fabricated by two consecutive L-PBF processes, as displayed in Fig. 1b. In the first process, a pure Ni powder with a nominal particle size distribution of 25–50 μm was used to produce the SX-like substrate [15]. In the subsequent process, the upper portion of the sample was deposited using HX powder with a particle size distribution of 10–45 μm. Firstly, the SX-like Ni substrates were fabricated on a SS304 build plate without preheated. The substrates were produced as cylinders specimens with a diameter of 12 mm and a height of 6 mm, with three specimens fabricated per built plate. The process parameters followed the method reported by Jodi et al. [15,16] for manufacturing SX pure Ni using L-PBF with flat-top laser beam, employing a laser power (P) = 500 W, scanning speed (V) = 140 mm/s, and hatch spacing (h) = 100 μm. After completion of the SX-like Ni substrates, the remaining Ni powder was removed, and both L-PBF chamber and the build plate were thoroughly cleaned. HX powder was then loaded into the hopper and the Ni substrate positions were kept unchanged. A 10 mm-tall HX structure was subsequently deposited on top of the SX-like Ni substrates. The HX samples were produced under three substrate preheating conditions, including without preheating (30 °C), 100 °C, and 200 °C. The layer thickness and hatch spacing were fixed at 30 and 100 μm, respectively, for all builds. The laser power and scanning speed were carried across three energy density (E) conditions,as shown in Table 2.

For HX deposited on SX-like Ni sample, specimens were sectioned vertically along the XZ plane (pararell to the build direction), mechanically polished, and then chemically etched using 10 %oxalic acid solution for both OM and SEM observations. For EBSD analysis, specimens were prepared using standard mechanical polishing and vibratory polishing techniques. EBSD data were acquired at an accelerating voltage of 15 kV and a step size of 7 μm. The crystallographic texture was quantified using the multiple of uniform distribution (MUD), where higher MUD values indicate a stronger preferred grain orientation. The MUD value significantly greater than 1 represent a pronounced texture in the L-PBF-processed HX samples.

2.3. Numerical simulation

To simulate the single-track behavior of polycrystalline HX substrate by the L-PBF process using flat-top laser (spot size 700 μm), the thermal field was calculated through a heat transfer model. A three-dimensional volumetric heat source model for flat-top laser was defined using a super-Gaussian distribution according to Coleman et al. [25]. The volumetric rate (Q) of energy input, Q is expressed in Equation (1), where η is the laser absorption coefficient of the material, P is the laser power and V_0 is the volume integral of the distribution. The terms Δx, Δy and Δz represent the x-, y- and z-components of the distance between a material point and the laser beam center, while $r_x(Z)$ and $r_y(Z)$ denote the distribution radii along the x- and y-directions, respectively. The parameter k defines the shape of the energy distribution. The variation of the distribution radius along the z-direction is described by Equation (2), where σ_i is the half-widths of the distribution, d is the depth of the heat source, and m represents the volumetric shape parameter. Furthermore, the volume integral of the distribution is given in Equation (3). The parameters k and m allow reproduction of a wide range of heat source distributions, where $k = m = 2$ corresponds to a conventional Gaussian ellipsoid distribution.

$$Q_{laser}(x,y,z)=\frac{\eta P}{V_0}\exp\left(\left[\frac{\Delta x^2}{r_x^2(z)}+\frac{\Delta y^2}{r_y^2(z)}\right]^{k/2}\right) \quad (1)$$

$$r_i(Z)=\frac{2\sigma_i}{\sqrt[k]{2}}\left(1-\left|\frac{\Delta z}{d}\right|^m\right)^{1/m}, i\in x,y \quad (2)$$

$$V_0=\pi\Gamma\left(1+\frac{2}{k}\right)\left(\frac{2\sigma_x}{\sqrt[k]{2}}\right)\left(\frac{2\sigma_y}{\sqrt[k]{2}}\right)d\left[\frac{\Gamma\left(1+\frac{1}{m}\right)\Gamma\left(1+\frac{2}{m}\right)}{\Gamma\left(1+\frac{3}{m}\right)}\right] \quad (3)$$

For single-track simulations, the heat transfer model consisted of a HX substrate without a powder bed. A computational domain of 4x2x2 mm in the x-, y-, and z-direction, respectively, was examined using a uniform mesh size of 20 μm. The simulations were performed under experimental conditions corresponding to low (P = 300 W, V = 200 mm/s), medium (P = 600 W, V = 200 mm/s), and high (P = 1000 W, V = 200 mm/s) energy densities, with varrying substrate preheating temperatures (without preheating, 100 °C, 200 °C, 300 °C, and 400 °C). The temperature-dependent thermophysical properties of HX alloy, including density, specific heat capacity and thermal conductivity, were followed by K.C. Mills [26]. The solidus and liquidus temperatures were set to T_S = 1533 K and T_L = 1628 K, respectively. The thermal history was calculate from the bottom of melt pool, including the G (K/m), R (m/s), and G × R (K/s).

3. Results and discussion

3.1. Melt pool morphology analysis

Fig. 2 shows the OM images of cross-sectional single-track melt pools without powder under various process parameters and substrate preheating temperatures. All melt pools exhibit a flat top, and their cross-sections display a semi-oval shape, which means it is deeper at the center and shallower near the edges. The melt pools generated by the flat-top laser beam are characterized by a significantly larger width compared to their depth. A statistical analysis of the melt pool dimensions was performed, and the results are presented in Fig. 3. Both the width and depth of the melt pool increase with higher LED, corresponding to higher P and lower V. As P increases from 300 to 1000 W, the melt pool width expands from approximately 550 to 805 μm at the same substrate preheating temperature. Similarly, the depth increases from about 60 to 210 μm. The melt pool width and depth demonstrate only minor variations with substrate preheating temperature, exhibiting a slight increasing trend at higher preheating levels. An increase in LED results in a larger and deeper melt pool, which reduces the temperature difference between the liquid and surrounding solid regions. This indicates that melt pool geometry is primarily governed by laser parameters rather than preheating conditions. The EBSD inverse pole figure (IPF) colour maps along the z-direction of the melt pool cross sections are presented in Fig. 4. Overall, equiaxed grains originating from the pre-existing the polycrystalline HX substrate propagate upward through the melt pool as the heat source advances. Base on the grain aspect ratio criterion proposed by Hunt [27], grains with a high aspect ratio (length (L)/distance (d) > 2) are classified as columnar, while those with ratio between 0 and 2 are categorized as equiaxed. Across all melt pool regions, including both columnar and equixed grains, the probability of columnar grain formation exceeds 70 %, as shown in Fig. 5. At high LED and substrate preheating conditions, the probability of columnar grains increases further, reaching up to 95 %. Partiality re-melted grains within the solidified structure align along G, which is generally parallel to the build direction, resulting in elongated grains with columnar morphology.

In addition, the primary microstructural difference among melt pools processed under various substrate preheating temperature is observed in the PDAS size. Fig. 6a-e show the dendritic microstructure at the center of melt pools under different preheating conditions at high LED. As illustrated in Fig. 6f, the mean PDAS increases with increasing energy density. Substrate preheating also promotes an increase in both the size and frequency of secondary dendrite arm spacing (SDAS). Under high LED, the mean PDAS increased from approximately 1.5 μm at 30 °C to 2.08 μm at substrate preheating at 400 °C. The PDAS size is strongly influenced by the local G × R during R and G present during processing [27]. To evaluate the capability of heat transfer simulations in accurately predicting the thermal history of the melt pool under various process parameters and preheating conditions, the variations in G, R, and G × R were analyzed, as shown in Fig. 7. With increasing LED, both G and R decrease, leading to a corresponding reduction in G × R. The experimentally observed PDAS followed a similar trend to the simulions (Fig. 6f), based on the established relation PDAS = 50 $(G \times R)^{-0.33}$ [28–30]. Likewise, increasing the substrate preheating temperature significantly reduces G, R and GxR, resulting in slow solidification and consequently larger PDAS values. However, the PDAS values from simulated results is slightly lower than those of experimental results. In the numerical simulation, GxR is determined by calculating the time interval between the liquidus and solidus temperatures at the center of the melt pool. Although the 3D volumetric heat-source model with a super-Gaussian distribution successfully reproduces the melt-pool width and depth [25,31], the calibration is based solely on transverse cross-sections. This approach lacks validation of longitudinal dimensions, providing only 2D thermal history information and neglecting fluid dynamics. This limitation leads to an overestimation of GxR during solidification in the finite difference method (FDM). In actual single-track experiments, the effective G × R is reduced by several

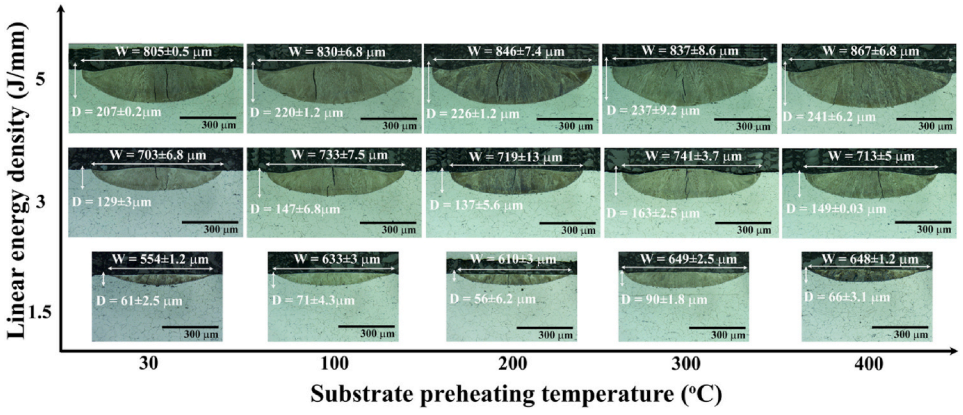

Fig. 2. OM images showing the cross-sectional melt pool morphologies on the polycrystalline HX substrates under various processing parameters and substrate preheating conditions.

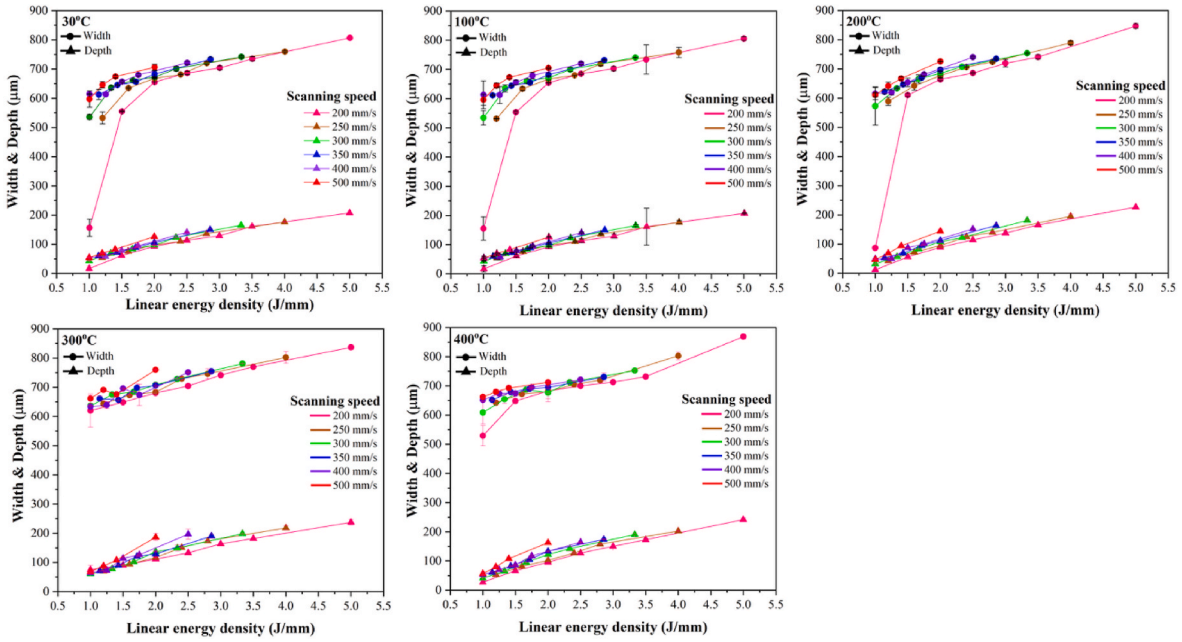

Fig. 3. Effect of process parameters and substrate preheating on melt pool dimension.

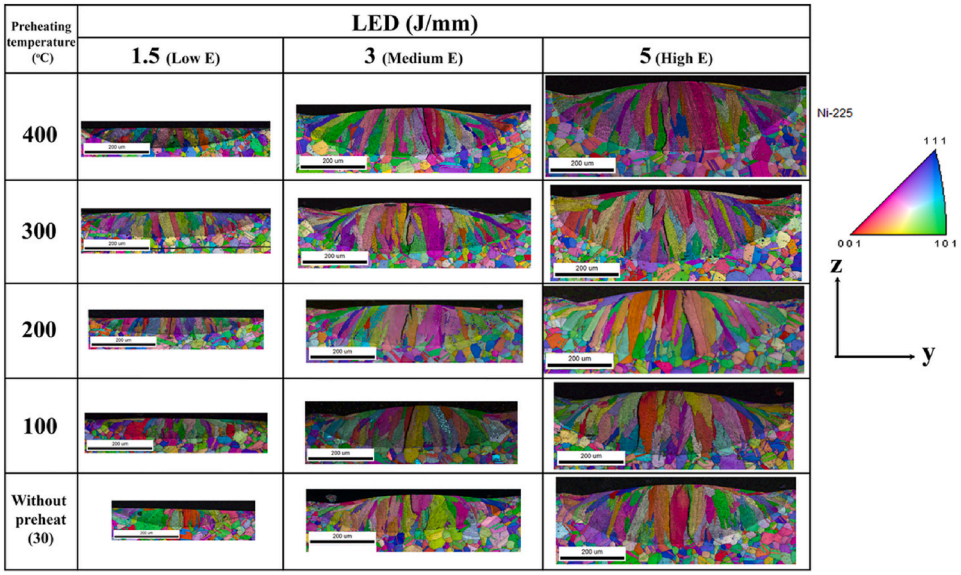

Fig. 4. IPF maps along Z-direction showing the variation of crystallographic texture as a function of LED and substrate preheating conditions.

factors, including melt-pool convection, transient thermal behavior during laser movement, and geometric effects inherent to the deposition process [32,33]. These factors decrease the actual G × R experienced by the material, allowing more time for dendrite coarsening. Consequently, experimentally measured PDAS values are typically larger than those predicted by simulation. These findings are consistent with previous reports by Zhang et al. [23] and Köhnen et al. [34]. It has been shown that lower LED increases both G and G × R, promoting microstructural refinement and reducing texture intensity. In contrast, substrate preheating decreases G and promotes the formation of deeper, elongated melt pools with lower R and reduced G × R [23,34]. Under such conditions, solidification proceeds more slowly, allowing additional time for dendrite arm growth and coarsening, which is evident as an increase in PDAS. This behavior highlights the significant influence of process parameters and thermal boundary conditions on PDAS. The trends observed in this study align closely with the heat transfer simulation results as well as prior experimental reports.

3.2. *Multi-tracks morphology analysis*

For multi-tracks results, variations in substrate preheating temperature did not produce statistically significant differences. However, at medium and high hatch spacing under both low and high area energy density (AED) conditions, larger gaps between adjacent tracks were observed, resulting in a wavy melt track bottom, as shown in Fig. 8. The insufficient overlap zone and relatively shallow melt pool depth are attributed to the reduced heat accumulation within the overlapping melt pool regions. Specifically, the melt pool depth decreased from 83 ± 7.5 to 56 ± 10 at low AED and from 270 ± 56 to 240 ± 16 at high AED. The alignment of columnar grains along the temperature gradient and the continuity of the melt pool are critical microstructural features that promote epitaxial growth from the underlying SX-like Ni substrate.

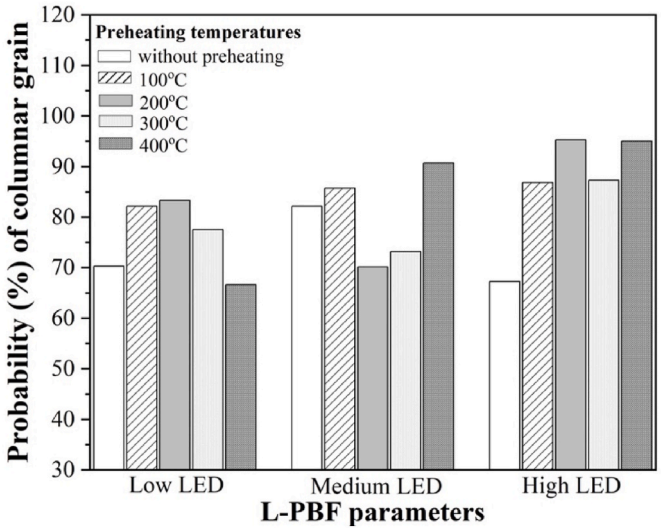

Fig. 5. Probability (%) of columnar grains in melt pool as a function of energy density and substrate preheating.

These characteristics facilitate the propagation of a preferred crystallographic orientation into the deposited HX layer. A decrease in hatch spacing can also contribute to dendrite coarsening, indicating a reduction in the local G × R due to changes in the G, as reported by Shao et al. [35]. Conversely, increasing the hatch spacing leads to a reduction in fabrication temperature and, a reduced G, which promotes heterogeneous nucleation and results in a weaker overall texture intensity [36]. Consequently, subsequent laser tracks cannot fully remelt and consolidate grains with different orientations. This prevents the preservation of elongated grains with a preferential crystallographic orientation. Furthermore, grains with diverse growth directions can develop, leading to an equiaxed solidification front and the formation of randomly oriented island grains.

3.3. *Effect of substrate preheating on interface between HX and SX-like Ni substrate*

Based on the single- and multi-track results, the L-PBF process parameters for fabricating cylindrical HX on SX-like Ni samples were selected using different combinations of both P and V, while maintaining a constant hatch spacing of 100 μm. It was observed that attempts to build HX at preheating temperature above 300 °C under high VED were unsuccessful. Excessive preheating leads to heat accumulation, resulting in elevated local temperatures in the upper regions. Because the previously deposited layers act as a thermally preheated base with high

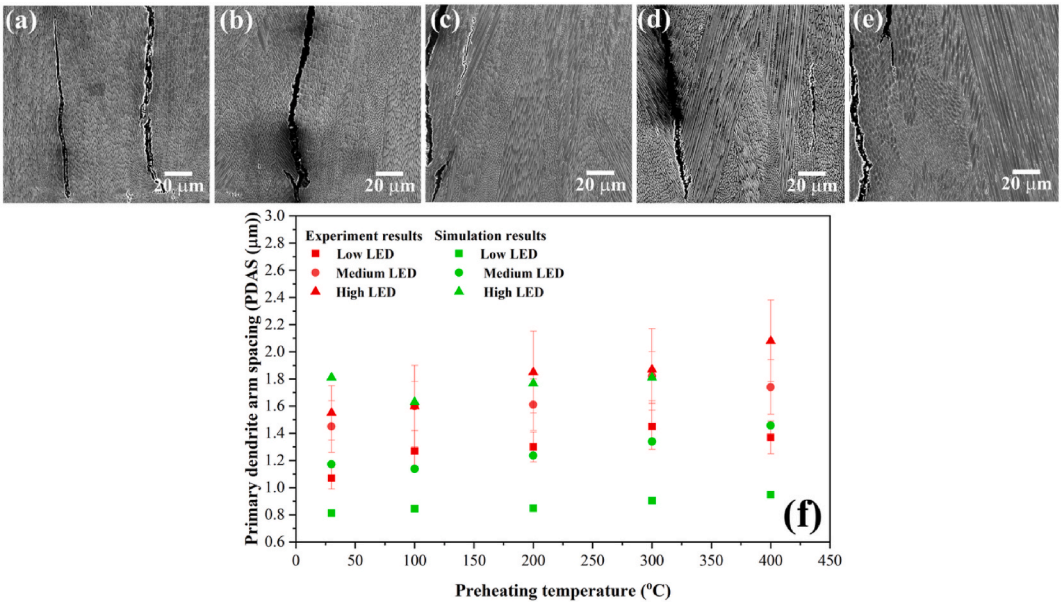

Fig. 6. SEM images showing elongated cell structures used for PDAS analysis in the melt pool under high LED conditions at different substrate preheating temperatures: (a) without preheating (30 °C), (b) 100 °C, (c) 200 °C, (d) 300 °C, (e) 400 °C, and (f) comparison of the mean experimental PDAS values with those predicted from the simulated G × R (Fig. 7) as a function of processing conditions.

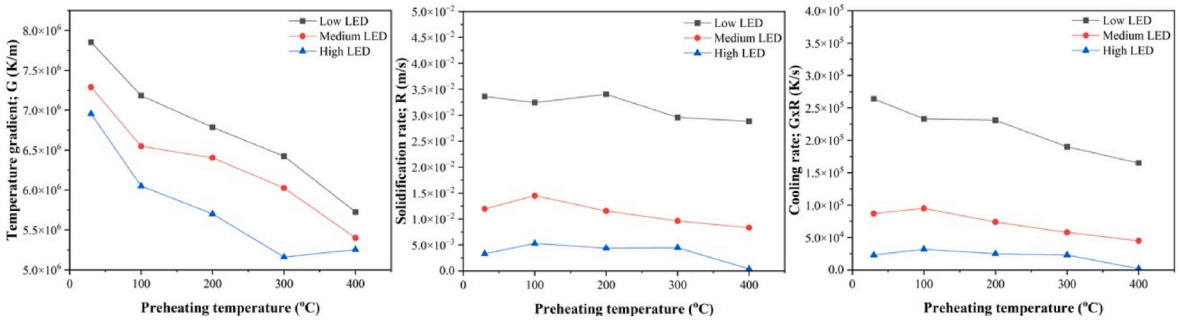

Fig. 7. Thermal history for various substrate preheating temperatures calculated using heat transfer model analysis.

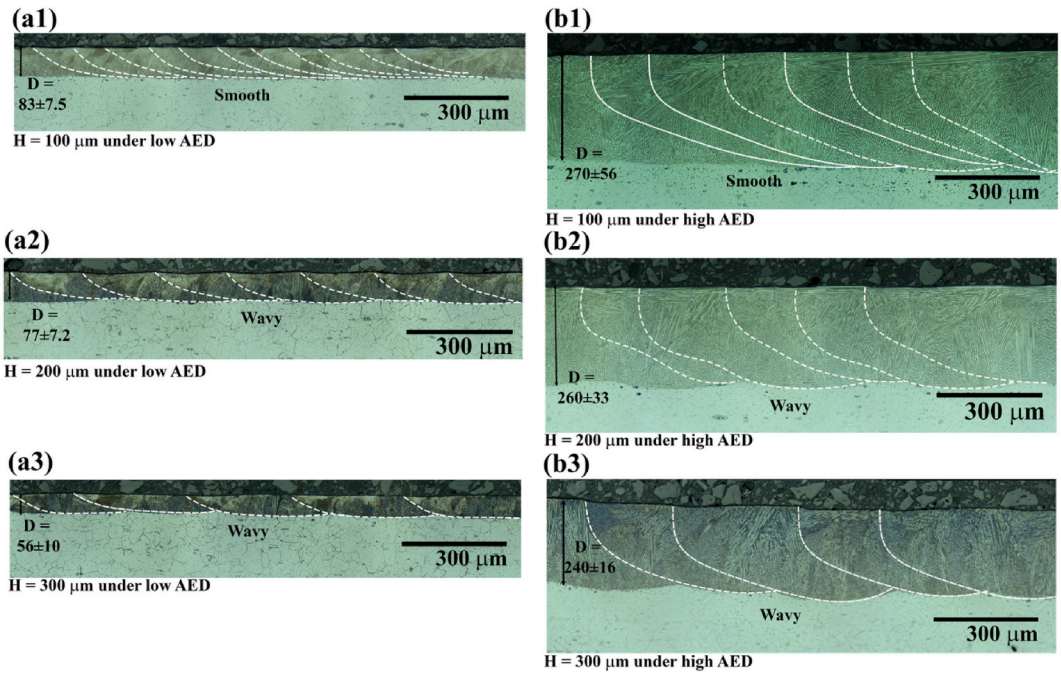

Fig. 8. OM images of etched cross-sections of multi-tracks on the polycrystalline HX substrate: (a) low AED and (b) high AED at substrate preheating temperature of 200 °C, with different hatch spacing of (1) 100 μm (2) 200 μm and (3) 300 μm.

overall thermal energy; consequently, the melt-pool temperature increases and its dimensions expand during subsequent passes. This can lead to swelling with a large contact angle due to the competition between surface tension and flow inertia. Such swelling may divide into irregular humps, further deteriorating surface roughness and contributing to part distortion or delamination, which ultimately results in complete build failure Consequently, the HX on SX-like Ni samples were fabricated using without substrate preheating (30), 100 and 200 °C.

Fig. 9 presents the interface region of low VED samples under different preheating temperatures. The results indicate that large pores are present at the interface when low preheating temperatures are used. This can result in poor adhesion between the HX layer and the SX-like substrate. As the preheating temperature increases, pore size decreases and bonding between the HX and SX-like substrate improves. This behavior is attributed to the combined effect of preheating and laser energy input, which increases the total energy input to the powder. Higher preheating temperatures reduce the additional energy required to melt the powder, thereby enhancing powder densification and improving bonding between the substrate and the deposited layer. Additionally, preheating decreases the amount of heat conducted from the deposited layer to the substrate, resulting in a lower G × R of the deposited layer. This delay in cooling suppresses the formation of interfacial flaws, thereby improving the metallurgical bond between the substrate and deposited material, as reported by Shim et al. [37]. Furthermore, variations in preheating temperature affect epitaxial growth and the orientation of columnar dendrites, with discontinuities observed at lower temperatures. Fig. 10 shows SE - SEM micrographs of etched samples, highlighting several microstructural features, including the epitaxial growth of the columnar grain aligned with build direction, extending from the Ni substrate through the HX deposited zone. Energy-dispersive spectroscopy (EDS) analysis of interface region allow clear identification of three distinct zones within deposited structure. The resulting microstructural features-particularly the alignment of columnar grains along G and the continuity of the melt pool-play a critical role in promoting epitaxial growth from the underlying SX-like Ni substrate, facilitating the propagation of a preferred crystallographic orientation into the deposited HX layer.

3.4. *Effect of substrate preheating on the crystallographic texture of HX and SX-like Ni substrate*

EBSD analysis was carried out on the L-PBF-fabricated HX on SX-like Ni cylindrical samples to investigate their crystallographic texture. Fig. 11 presents the IPF orientation maps obtained from the XZ plane along the Z-direction corresponding {001} pole figures under different process parameters. As shown in Fig. 11, the IPF maps are predominantly red, indicating a strong <100> fiber texture of the FCC crystal structure aligned parallel to the build direction. The evolution of strong texture with <001> aligned along the Z-direction. Samples fabricated under high VED exhibit a more pronounced <001> texture and larger

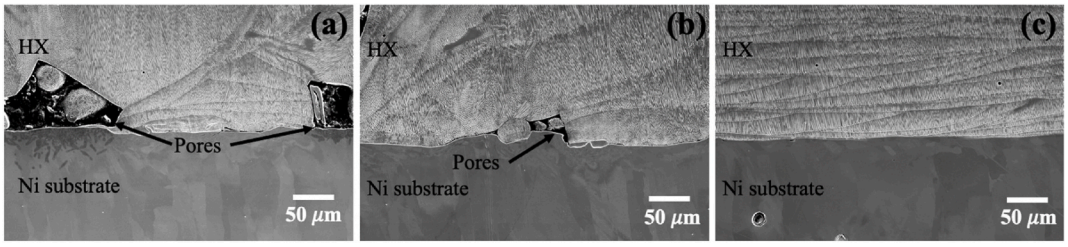

Fig. 9. SE - SEM images of the interface between HX layers and the Ni substrate prepared at low E with substrate preheating of (a) without preheating, (b) 100 °C, and (c) 200 °C.

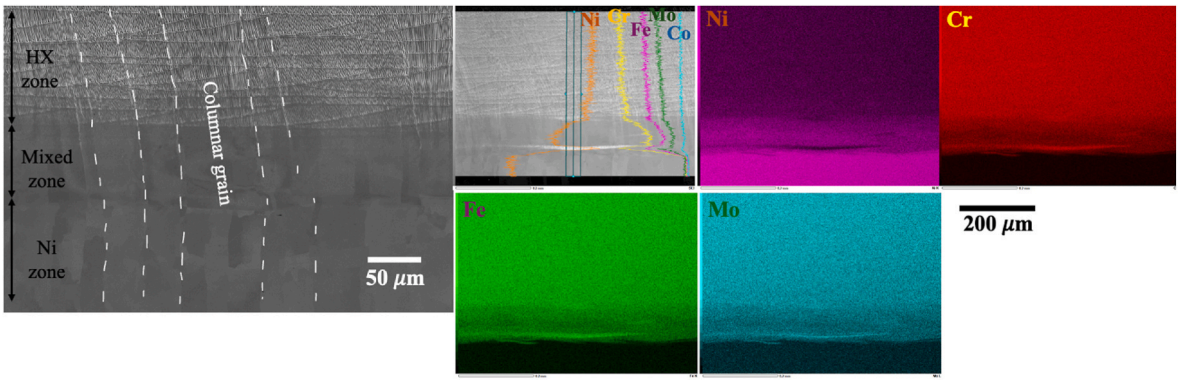

Fig. 10. Detail view of the interface region in the HX on SX-like Ni sample, showing three distinct regions together with line and mapping EDS analyses.

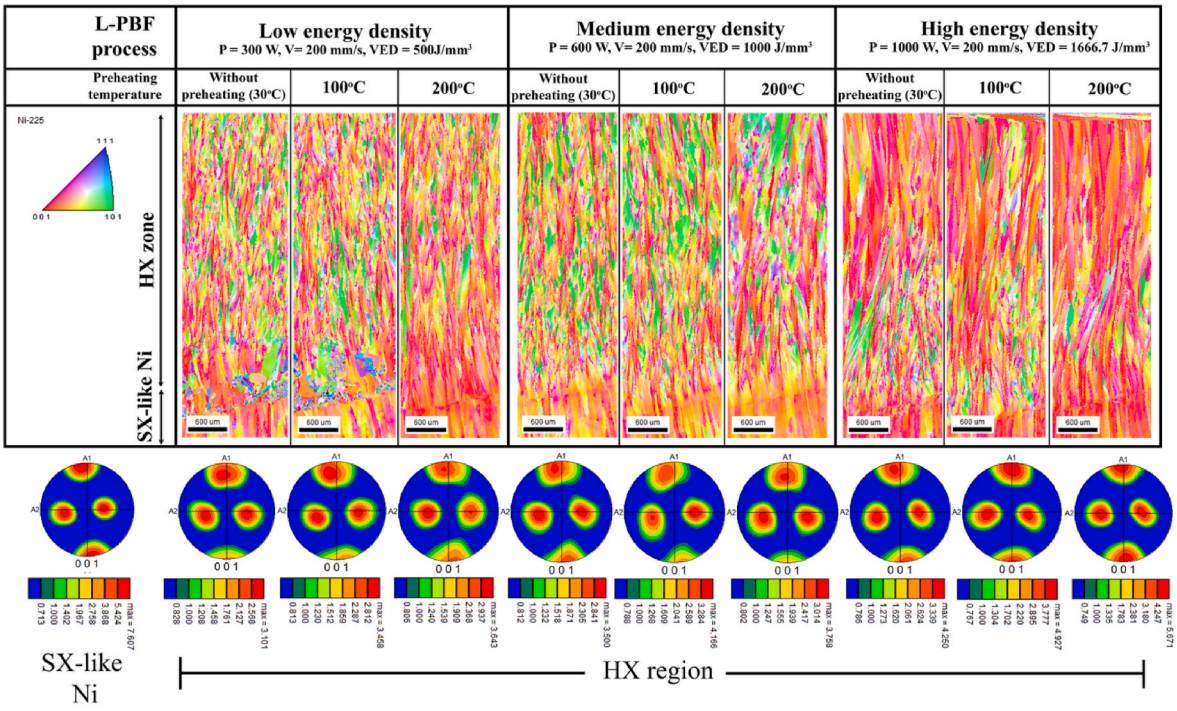

Fig. 11. IPF maps showing the crystallographic texture corresponding {001} pole figure along the Z-direction of HX on SX-like Ni samples under different processing parameters.

columnar grain structures aligned with the build direction compared to those produced under low and medium VED conditions. Regarding substrate preheating, HX samples processed at 200 °C show a significant enhancement in crystallographic texture relative to lower preheating temperatures. Specifically, the 200 °C samples display the strongest <001> textures across all VED conditions with the MUD intensity of approximately 3–4, as shown in Fig. 12. Moreover, average grain size of the low VED sample without substrate preheating was 105 ± 20 μm, while increasing to 236 ± 46 μm when increasing substrate preheating at 200 °C. Despite the same tendency, the average grain size of the medium and high VED samples was higher than the low VED sample at the same substrate preheating temperature, as shown in Fig. 13. Local substrate preheating promotes higher energy retention per layer, resulting in melt pools that are both wider and deeper. Under high VED conditions with substrate preheating, the temperature gradient becomes more uniform and aligned along the build direction. This indicates that solidification proceeds more slowly and stably, thereby enhancing epitaxial grain growth and the orientation of columnar dendrites. In contrast, discontinuities in grain orientation are more evident at lower preheating temperatures, consistent with observations reported by Liu et al. [21] and Chen et al. [22]. Furthermore, the combination of optimized laser parameters and substrate preheating helps stabilize G and reduces localized GxR, thereby enhancing epitaxial grain propagation and grain size along with promoting the development of a uniform SX-like microstructure in the deposited HX material.

3.5. *Effect of processing parameters on the crystallographic texture of HX deposited layer*

Fig. 14 presents the processing map plotted based on the maximum values of the <001> texture, expressed as the MUD intensity, for the HX region at a constant preheating temperature of 200 °C. The results indicate that increasing the scanning speed and decreasing the laser power weaken the development of the <001> texture. The strongest <001> texture was observed in samples fabricated with a scanning speed of 200–350 mm/s and a laser power of 1000 W. At higher VED, the melt pool temperature rise and its dimensions enlarge, extending the melt pool lifetime and reducing the G, R and G × R, as discussed in

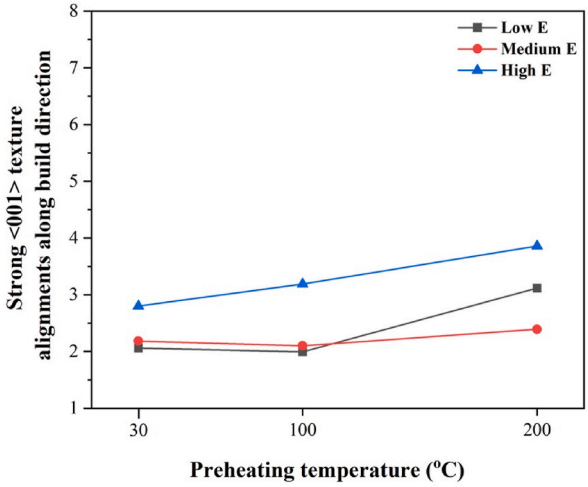

Fig. 12. The <001> textures intensity (MUD value) of the HX region fabricated under various energy densities and substrate preheating conditions.

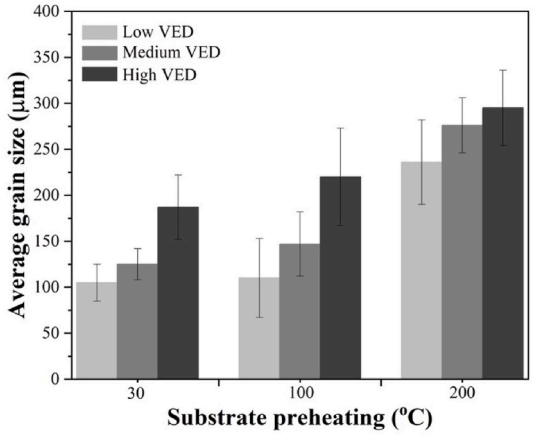

Fig. 13. Average grain size in build HX region as a function of energy density and substrate preheating.

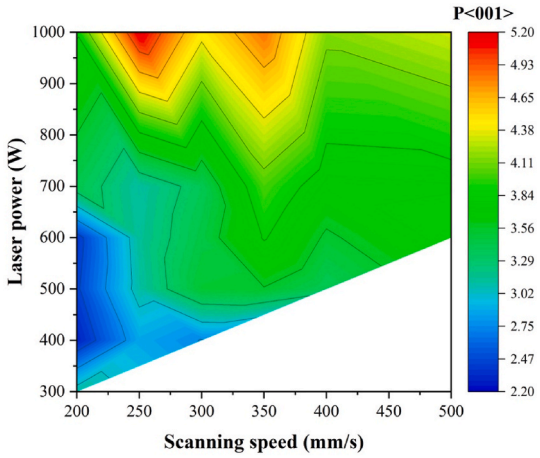

Fig. 14. The <001> textures intensity (MUD value) of the HX region fabricated under various laser powers and scanning speeds at substrate preheating temperature of 200 °C along the build direction.

section 3.1. Under these slower solidification conditions, heat extraction is dominated by conduction into the SX substrate, which stabilizes the solid-liquid interface. This condition suppresses heterogeneous nucleation in the melt and favors competitive dendritic growth aligned with the substrate's < 001> orientation. Consequently, epitaxial grain propagation is promoted, enabling the substrate orientation to transfer into successive HX layers and facilitating the formation of extended columnar grains. In contrast, faster solidification front under lower VED conditions destabilizes the epitaxial interface, increasing the likelihood of stray grain nucleation, misorientation, and local texture discontinuities. These effects collectively weaken epitaxial growth and result in mixed or weaker textures.

3.6. Formation of stray grains in HX deposited on SX-like Ni substrate

The texture transition behavior was systematically examined at the initial stage of deposition, as shown in Fig. 15. The results reveal the IPF maps together with the corresponding variations in the <001> crystal orientation on the XZ plane along the Z-direction. Under all processing conditions, the <001> orientation profiles exhibited values higher than those of a randomly oriented polycrystalline reference (MUD <1). Nevertheless, the MUD values decreased after the deposition of HX layers in all conditions. Fig. 16a illustrates the variation of MUD values as a function of deposition height. Within the substrate region, the peak MUD reaches values of 7–8. Beyond this region, the <001> texture exhibited a pronounced decrease at the substrate-deposited interface. In the HX region adjacent to the substrate, the MUD values initially decreased but subsequently increased with build height, eventually stabilizing at approximately 4.5–5. This behavior indicates a deviation in the preferred crystallographic orientation, which disrupts epitaxial growth and promotes the formation of stray grains. Stray grains were observed in the HX deposited zone, leading to the formation of distinct high-angle grain boundaries (HABs). The occurrence of these stray grains in the HX region can be attributed to several factors [38–43]. At high magnification near interface (Fig. 16b), this microstructural evolution can be attributed to epitaxial growth originating from the pre-existing SX-like Ni substrate, extending through the remelting zone into the first deposited HX layer, as confirmed by the EBSD analysis of the interface region (IPF, grain and rotation angle maps). It is evident that each columnar grain exhibits a consistent color in both the substrate and the re-melted zone, indicating that the crystal orientation is preserved across these regions. In SX-like Ni substrate, no high angle boundary (HAGBs, marked as blue lines) were observed; however, low-angle grain boundaries (LAGBs, indicated as yellow and red lines) were still present. The orientation was not strictly aligned with the <001> direction, and fluctuations in the original orientation became more pronounced with increasing build height. The LAGBs misorientation angles were close to the deviation angles between adjacent grains. Fig. 16c shows the etched SE - SEM image at the interface through the HX deposited region. Stray grains appeared during the competitive growth of the HX layer near the remelting interface. Dendrites were also observed in the HX deposited layers, but their orientation deviated from that of the seed grains. For instance, the preferred orientation of the primary dendrite arms <001> originating from the SX-like Ni seed through the remelting region was found to deviated by approximately 8o and 15o from the growth direction. The first HX deposited layer was formed through the simultaneous melting and solidification of the powder and the underlying substrate under processing conditions distinct from those used to fabricate the SX-like Ni substrate. In this HX layer, the preferred orientation of columnar cells was aligned with the direction of heat transfer, reflecting the temperature gradient that governed solidification. As solidification progressed, the orientation of these cellular grains gradually adjusted, attempting to realign toward the primary growth direction dictated by the evolving temperature gradient. This adjustment was strongly influenced by the shape of the HX melt pool, which differed from that of the Ni substrate, as shown in schematically diagram in Fig. 17. This explains the observed inclination of cellular grains within the remelted region of the HX deposited layer,

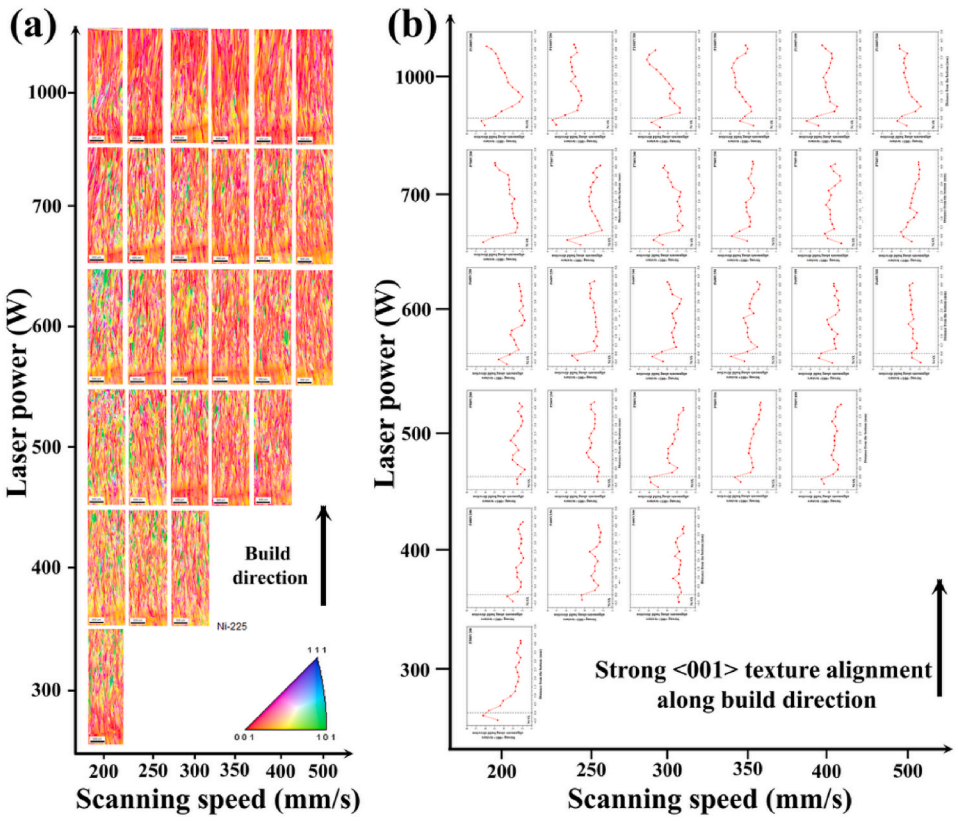

Fig. 15. (a) IPF orientation maps of L-PBF fabricated HX on SX-like Ni under various process conditions at a substrate preheating temperature of 200 °C, and (b) variation in the <001> textures intensity with different process parameters at 200 °C through build direction.

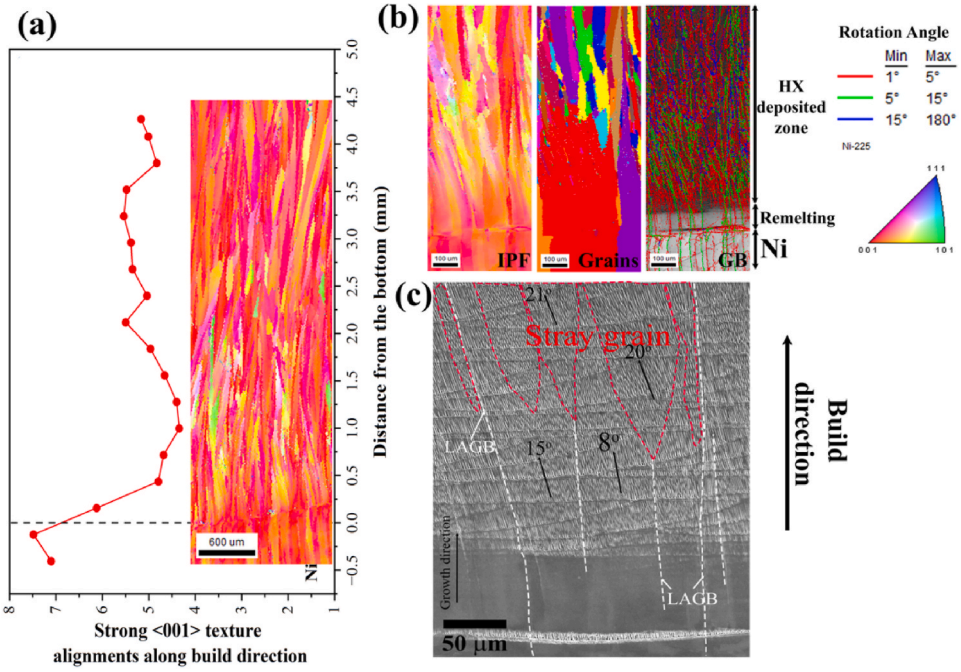

Fig. 16. (a) IPF orientation maps and variation in <001> textures along the Z-direction of L-PBF fabricated HX on SX-like Ni substrate and enlarged views of internal interfaces: (b) EBSD maps, including IPF, grain and rotation angle maps, with (c) the corresponding SE - SEM image indicating the origin of stray grain growth.

where the altered melt pool geometry redirected the growth trajectory away from the ideal vertical <001> orientation. Such behavior contrasts with that observed in SX substrates produced by casting techniques, where crystal orientation are more favorable for maintaining epitaxial alignment [8,18,20,39,43]. Moreover, stray grains were observed at the LABs between two grains, particularly at the divergence ends of dendrite crystals. These stray grain exhibited relatively small deviation angles between the cellular growth direction and the heat flow

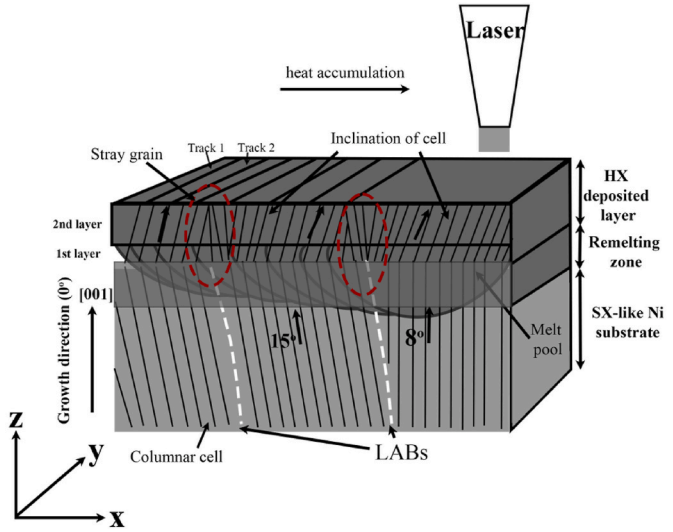

Fig. 17. Schematic diagram showing the inclination of cellular grains on HX deposited layers.

direction. Zhou [38] also reported that stray grains tend to form at both diverging and converging grain boundaries during directional solidification of SX Ni-based superalloy. LABs separate individual dendrites or small dendrite groups, and stray grains preferentially nucleate and grow from converging boundaries due to the lower melting temperature of interdendritic regions caused by elemental segregation, similar to observations in laser directed solidification of single crystal superalloys by Wang et al. [39]. These finding confirm that LABs in the SX-like Ni substrate play a critical role in disrupting epitaxial growth from the substrate, thereby facilitating the nucleation of stray grains within the HX deposited layer. Consequently, the presence of stray grains interrupts the continuity of the <001> texture, reducing the overall sharpness of crystallographic alignment and weakening the desired single-crystal-like microstructure. Moreover, the compositional mismatch between HX and pure Ni significantly influence stray grain formation by modifying solidification behavior. During rapid solidification, elemental segregation especially of Mo, Cr, and Fe in the HX alloy, leads to local compositional fluctuations that reduce the stability of the solidification front and promote heterogeneous nucleation of equiaxed grains. In laser remelting studies of directionally solidified Ni-based superalloys, stray grains were frequently observed near fusion lines where segregation of refractory elements and eutectic/carbide phases occurs, lowering local melting temperatures and inducing constitutional undercooling, as reported by Lei et al. [40] and Liu et al. [41]. The crystallographic stability with respect to both the process parameters and the substrate crystal orientation plays a critical role in enhancing the continuity of epitaxial columnar dendrites. The texture transition behavior at the initial stage of deposition is also important in the deposited L-PBF process.

4. Conclusions

The effects of substrate preheating and processing parameters on the crystallographic texture of HX deposited on SX-like Ni substrates were systematically investigated. The following conclusions can be drawn:

4.1 The melt pool morphology was primarily governed by the L-PBF process. Higher P and lower V produced larger melt pools, while substrate preheating had only a minor effect. A high LED combined with substrate preheating reduced G, R, and G × R during single-track solidification, promoting slower and more stable growth that increased both the fraction of columnar grains and the mean PDAS size.

4.2 In multi-track experiments, the smallest H (100 μm) generated straight and uniform melt pool boundaries, enhancing heat accumulation, consistent remelting, and epitaxial growth between adjacent tracks.

4.3 Substrate preheating also improved metallurgical bonding by reducing interfacial porosity, lowering G × R, and enhancing powder densification, thereby facilitated the propagation of the preferred <001> crystallographic orientation from the substrate into the deposited HX layer.

4.4 Overall, high VED combined with substrate preheating at 200 °C stabilized G value, slowed solidification, and promoted epitaxial grain growth, resulting in a more uniform SX-like microstructure.

4.5 The inclination of cellular grains and the formation of stray grains during competitive growth near the interface were influenced by the substrate orientation and the presence of low-angle grain boundaries (LABs), which affected the continuity of the <001> texture.

Importantly, stray grains disrupt the SX-like structure, leading to local deviations in crystallographic orientation that can degrade high-temperature strength, creep resistance, and fatigue performance.

Declaration of competing interest

The authors declare that they have no known competing financial interests or personal relationships that could have appeared to influence the work reported in this paper.

Acknowledgments

This work was supported by “Innovative Science and Technology Initiative for Security, Grant Number JPJ004596 implemented by the Acquisition, Technology, and Logistics Agency (ATLA), Japan” and “The Amada Foundation, Grant Number AF-2022201-A3”.

References

[1] Han Q, Mertens R, Montero-Sistiaga ML, Yang S, Setchi R, Vanmeensel K, Hooreweder BV, Evans SL, Fan H. Laser powder bed fusion of hastelloy X: effects of hot isostatic pressing and the hot cracking mechanism, mater. Sci Eng A 2018;732:228–39. https://doi.org/10.1016/j.msea.2018.07.008.

[2] Esmaeilizadeh R, Keshavarzkermani A, Ali U, Mahmoodkhani Y, Behravesh B, Jahed H, Bonakdar A, Toyserkani E. Customizing mechanical properties of additively manufactured hastelloy X parts by adjusting laser scanning speed. J Alloys Compd 2020;812:152097. https://doi.org/10.1016/j.jallcom.2019.152097.

[3] Bai J, Ma R, Zhang Y, Cheng L, Wang Y, Zhou W. Effect of laser power and heat treatment on microstructures and tensile properties of LPBF fabricated hastelloy X superalloy. Mater Res Express 2023;10:106515. https://doi.org/10.1088/2053-1591/acff3f.

[4] Hibino S, Todo T, Ishimoto T, Gokcekaya O, Koizumi Y, Igashira K, Nakano T. Control of crystallographic texture and mechanical properties of hastelloy-X via laser powder bed fusion. Crystals 2021;11(9):1064. https://doi.org/10.3390/cryst11091064.

[5] Hagihara K, Nakano T. Control of anisotropic crystallographic texture in powder bed fusion additive manufacturing of metals and ceramics-a review. J Min Met Mater S 2022;73:1760–73. https://doi.org/10.1007/s11837-021-04966-7.

[6] Kou S. Welding metallurgy. second ed. Wiley-Interscience; 2003.

[7] Gäumann M, Bezençon C, Canalis P, Kurz W. Single-crystal laser deposition of superalloys: processing-microstructure maps. Acta Mater 2001;49:1051–62. https://doi.org/10.1016/S1359-6454(00)00367-0.

[8] Chauvet E, Tassin C, Blandin J-J, Dendievel R, Martin G. Producing Ni-base superalloys single crystal by selective electron beam melting. Scr Mater 2018;152:15–9. https://doi.org/10.1016/j.scriptamat.2018.03.041.

[9] Dinda GP, Dasgupta AK, Mazumder J. Texture control during laser deposition of nickel-based superalloy. Scr Mater 2012;67:503–6. https://doi.org/10.1016/j.scriptamat.2012.06.014.

[10] Sun S-H, Hagihara K, Nakano T. Effect of scanning strategy on texture formation in Ni-25 at.%Mo alloys fabricated by selective laser melting. Mater Des 2018;140:307–16. https://doi.org/10.1016/j.matdes.2017.11.060.

[11] Liang Y-J, Li J, Li A, Cheng X, Wang S, Wang HM. Experimental optimization of laser additive manufacturing process of single-crystal nickel-base superalloys by a statistical experiment design method. J Alloys Compd 2017;697:174–81. https://doi.org/10.1016/j.jallcom.2016.12.109.

[12] Daram P, Kusano M, Watanabe M. Investigation of the process optimization for L-PBF hastelloy X alloy on microstructure and mechanical properties. Materials 2025;18(8):1890. https://doi.org/10.3390/ma18081890.
[13] Montero-Sistiaga ML, Pourbabak S, Humbeeck JV, Schryvers D, Vanmeensel K. Microstructure and mechanical properties of Hastelloy X produced by HP-SLM (high power selective laser melting). Mater Des 2019;165:107598. https://doi.org/10.1016/j.matdes.2019.107598.
[14] Jodi DE, Kitashima T, Singh A, Watanabe M. High-temperature microstructural stability of pure Ni fabricated by laser powder bed fusion using Gaussian and flat-top beam profiles. Mater Char 2023;200:112897. https://doi.org/10.1016/j.matchar.2023.112897.
[15] Jodi DE, Kitashima T, Koizumi Y, Nakano T, Watanabe M. Manufacturing single crystals of pure nickel via selective laser melting with a flat-top laser beam. Addit Manuf Lett 2022;3:100066. https://doi.org/10.1016/j.addlet.2022.100066.
[16] Jodi DE, Kitashima T, Watanabe M. Effect of scan strategy on the formation of a pure nickel single-crystal structure using a flat-top laser beam via laser powder bed fusion. Sci Technol Adv Mater 2023;24:2201380. https://doi.org/10.1080/14686996.2023.2201380.
[17] Xue J, Zhang A, Li Y, Qian D, Wan J, Qi B, Tamura N, Song Z, Chen K. A synchrotron study of microstructure gradient in laser additively formed epitaxial Ni-based superalloy. Sci Rep 2015;5:14903. https://doi.org/10.1038/srep14903.
[18] Ishimoto T, Hagihara K, Hisamoto K, Nakano T. Stability of crystallographic texture in laser powder bed fusion: understanding the competition of crystal growth using a single crystalline seed. Addit Manuf 2021;43:102004. https://doi.org/10.1016/j.addma.2021.102004.
[19] Adegoke O, Andersson J, Brodin H, Pederson R. Review of laser powder bed fusion of gamma-prime-strengthened nickel-based superalloys. Materials 2020;10(8):996. https://doi.org/10.3390/met10080996.
[20] Liu Z, Shu J. Characterization of microstructure, precipitations and microsegregation in laser additive manufactured nickel-based single-crystal superalloy. Materials 2010;13(10):2300. https://doi.org/10.3390/ma13102300.
[21] Liu Z, Wang Z. Effect of substrate preset temperature on crystal growth and microstructure formation in laser powder deposition of single-crystal superalloy. J Mater Sci Technol 2018;34:2116–24. https://doi.org/10.1016/j.jmst.2018.04.016.
[22] Chen Y, Wang W, Ou Y, Li D, Chang H, Wu Y, Yang R, Zhai Z, Li C. Effect of high preheating on the microstructure and mechanical properties of high gamma prime Ni-based superalloy manufactured by laser powder bed fusion. J Alloys Compd 2023;960:170598. https://doi.org/10.1016/j.jallcom.2023.170598.
[23] Zhang F, Zhou L, Xie X, Zhang Z, Chao Q, Fan G. Crack inhibition and crystallographic texture control in an additively manufactured IN738LC Ni-based superalloy. J Mater Sci Technol 2024;33:652–66. https://doi.org/10.1016/j.jmrt.2024.09.101.
[24] Park J-H, Bang GB, Lee K-A, Son Y, Song YH, Lee B-S, Kim WR, Kim HG. Effect of preheating temperature on microstructural and mechanical properties of inconel 718 fabricated by selective laser melting. Met Mater Int 2022;28:2836–48. https://doi.org/10.1007/s12540-022-01169-w.
[25] Coleman J, Knapp GL, Stump B, Stoyanov M, Plotkowski A. A dynamic volumetric heat source model for laser additive manufacturing. Addit Manf 2024;95:104531. https://doi.org/10.1016/j.addma.2024.104531.
[26] Mills KC. Recommended values of thermophysical properties for selected commercial alloys. Woodhesd; 2002.
[27] Harrison NJ, Todd I, Mumtaz K. Reduction of micro-cracking in nickel superalloys processed by selective laser melting: a fundamental alloy design approach. Acta Mater 2015;94:59–68. https://doi.org/10.1016/j.actamat.2015.04.035.
[28] Kusano M, Takata Y, Yumoto A, Watanabe M. Effects of time per layer and part geometry on thermal history and microcracking in the fabrication of nickel superalloy samples by laser powder bed fusion. Addit Manuf 2024;80:103987. https://doi.org/10.1016/j.addma.2024.103987.
[29] Jena A, Atabay SE, Brochu M. Microstructure and mechanical properties of crack-free Inconel 738 fabricated by laser powder bed fusion. Mater Sci Eng 2022;850:143524. https://doi.org/10.1016/j.msea.2022.143524.
[30] Li S, Wei Q, Shi Y, Chua CK, Zhu Z, Zhang D. Microstructure characteristics of Inconel 625 superalloy manufactured by selective laser melting. J Mater Sci Technol 2015;31:946–52. https://doi.org/10.1016/j.jmst.2014.09.020.
[31] Briffod F, Daram P, Kusano M, Watanabe M. An integrated computational materials engineering framework for process–structure–property mapping in laser powder bed fusion. Mater Des 2025;260:115097. https://doi.org/10.1016/j.matdes.2025.115097.
[32] Cauwenbergh PV, Samaee V, Thijs L, Nejezchlebová J, Sedlák P, Iveković A, Schryvers D, Hooreweder BV, Vanmeensel K. Unravelling the multi-scale structure–property relationship of laser powder bed fusion processed and heat-treated AlSi10Mg. Sci Rep 2021;11:6423. https://doi.org/10.1038/s41598-021-85047-2.
[33] Sabau AS, Yuan L, Raghavan N, Bement M, Simunovic S, Turner JA, Gupta VK. Fluid dynamics effects on microstructure prediction in single-laser tracks for additive manufacturing of IN625. Metall Mater Trans B 2020;51:1263–81. https://doi.org/10.1007/s11663-020-01808-w.
[34] Köhnen P, Létang M, Voshage M, Schleifenbaum JH, Haase C. Understanding the process-microstructure correlations for tailoring the mechanical properties of L-PBF produced austenitic advanced high strength steel. Addit Manuf 2019;30:100914. https://doi.org/10.1016/j.addma.2019.100914.
[35] Shao W, He B, Qiua C, Li Z. Effect of hatch spacing and laser remelting on the formation of unique crystallographic texture of IN718 superalloy fabricated via laser powder bed fusion. Opt Laser Technol 2022;156:108609. https://doi.org/10.1016/j.optlastec.2022.108609.
[36] Saghaian SE, Nematollahi M, Toker G, Hinojos A, Moghaddam NS, Saedi S, Lu CY, Mahtabi MJ, Mills MJ, Elahinia M, Karaca HE. Effect of hatch spacing and laser power on microstructure, texture, and thermomechanical properties of laser powder bed fusion (L-PBF) additively manufactured NiTi. Opt Laser Technol 2022;149:10768. https://doi.org/10.1016/j.optlastec.2021.107680.
[37] Shim D-S, Lee K-Y, Park S-H. Bending strength of tool steel preheated to various temperatures and layered by direct energy deposition. Mater Sci Eng 2019;744:548–59. https://doi.org/10.1016/j.msea.2018.12.009.
[38] Zhou Y. Formation of stray grains during directional solidification of a nickel-based superalloy. Scr Mater 2011;65:281–4. https://doi.org/10.1016/j.scriptamat.2011.04.023.
[39] Wang J, Wang H, Li K, Chen M, Zhang M, Zhang B, Yuan J, Cheng X, Zhang S, Wang Y. A new strategy to inhibit stray grain formation during laser directed solidification of single crystal superalloys. J Alloys Compd 2022;906:163852. https://doi.org/10.1016/j.jallcom.2022.163852.
[40] Lei Z, Lu N, Yu X. Epitaxy and new stray grain formation mechanism during epitaxial laser melting deposition of Inconel 718 on directionally solidified nickel-based superalloys. J Manuf Process 2019;42:11–9. https://doi.org/10.1016/j.jmapro.2019.04.016.
[41] Liu G, Du D, Wang K, Pu Z, Chang B. Epitaxial growth behavior and stray grains formation mechanism during laser surface re-melting of directionally solidified nickel-based superalloys. J Alloys Compd 2021;853:157325. https://doi.org/10.1016/j.jallcom.2020.157325.
[42] Wang F, Liu Y, Yang Q, Ma D, Li D. Microscale stray grains formation in single-crystal turbine blades of Ni-based superalloys. J Mater Sci Technol 2024;191:134–45. https://doi.org/10.1016/j.jmst.2024.01.012.
[43] Guan W, Chen C, Pan X, Zhao R, Lu X, Hu T, Xu S, Xuan W, Panwisawas C, Lei L, Wang J, Ren Z. On the control of epitaxial growth and stray grains during laser-directed energy deposited Ni-based single crystal superalloy. Mater Char 2024;212:113969. https://doi.org/10.1016/j.matchar.2024.113969.